Bipolar Checkerboard Metal Object Detection Without Blind Zone Caused by Excitation Magnetic Field for Stationary EV Wireless Charging System

Shuze Zhao, Chenyang Xia, *Member, IEEE*, Ziyue Yang, Hao Lu, Hongtai Zhang, and Chenhao Lu

***Abstract*—Metal object detection (MOD) technology provides a guarantee for the safe operation of electric vehicle (EV) wireless charging system. To solve the problem of detection blind zone caused by excitation magnetic field in the existing MOD technology, a bipolar checkerboard MOD technology is proposed. By adding an excitation source, not only the blind zone is eliminated but also it makes the EV wireless charging system and the MOD system work independently. First, the positions and causes of the blind spot caused by the excitation magnetic field of the Tx coil in the EV wireless charging system are analyzed. Second, the structure and principle of the bipolar checkerboard MOD system are analyzed. Third, a definition of the detection sensitivity of MOD is given, and the relationship between sensitivity and the size parameters of bipolar checkerboard sensing coil sets is analyzed. Moreover, the parameter optimization method of the sensing coil sets and detection circuit is analyzed. Finally, a MOD system experimental setup is built to verify its feasibility. The results show that the highest sensitivity can reach 20% for a square aluminum plate of $80 \times 80 \times 1$ mm^3 without a blind zone and the two systems can work independently with each other.**

***Index Terms*—Bipolar checkerboard, blind zone, electric vehicle (EV) wireless charging, independent work, metal object detection (MOD).**

I. Introduction

DUE to the advantages of zero emission and zero pollution, electric vehicle (EV) is gaining widespread attention and its global market share is increasing rapidly. The magnetic field coupled wireless charging technology provides a more safe and convenient way to replenish energy for EVs [1], [2], [3], [4], [5]. To promote the industrialization of EVs wireless charging technology, four wireless charging standards for EVs: IEC 61980, SAE J2954, ISO 19363, and GB/T 38775 have been developed in many countries around the world [6], [7], [8], [9]. Furthermore, they have been continuously updated and improved.

With the continuous development and progress of EVs wireless charging technology, the requirements for safety performance during its charging process are becoming higher and higher. Therefore, foreign object detection technology is specified in detail in the EV wireless charging standard, which includes metal object detection (MOD) and living object detection [10], [11]. Since there is a high-frequency electromagnetic field between the transmitting (Tx) coil and receiver (Rx) coil of the EV wireless charging system, eddy currents will be generated inside the metal objects (MOs) that appear in the high-frequency electromagnetic field. Thus, it can affect the transmission power and efficiency, whereas there is also a fire risk due to the heat generation problem caused by MOs' eddy currents [12], [13], [14], [15], [16]. Therefore, MOD technology has received extensive research and attention.

Existing MOD methods include detection techniques based on magnetoresistive sensors [17], ultrasonic radar [11], wireless charging system parameters [18], [19], sensing coils [20], [21], [22], [23], [24], [25], [26], [27], etc. Among them, the MOD method based on wireless charging system parameters and sensing coils has the advantages of simple principle, low cost, and high reliability.

For the MOD method based on the parameters of the wireless charging system, the literature [18] proposes a method for MOD by detecting the fifth harmonic current amplitude of the Tx coil. A method for MOD by detecting the deviation of the Tx coil current amplitude and the resonant frequency is proposed in the literature [19]. Compare with the MOD method based on sensing coils, the method based on wireless charging system parameters does not require additional coil sets structure. However, due to the advantages of high detection sensitivity and scalability of auxiliary functions, the detection method based on sensing coils has become the mainstream technology of current research.

For the MOD method based on sensing coils, a dual-purpose nonoverlapping coil sets structure is proposed in the literature [20], which enables MOD and detection of position (DoP) by detecting the amplitude of the induced voltage in the coil sets. In the literature [21], a double-layer symmetrical coil sets structure is proposed that can realize the MOD position determination function. This type of MOD method is based on passive sensing coils, using Tx coil to generate MOD excitation magnetic field,

Manuscript received 19 September 2022; revised 8 December 2022; accepted 6 January 2023. Date of publication 23 January 2023; date of current version 10 March 2023. This work was supported in part by the National Natural Science Foundation of China under Grant 52277020 and in part by the Natural Science Foundation of Jiangsu Province under Grant BK20211246. Recommended for publication by Associate Editor J. Acero. *(Corresponding author: Chenyang Xia.)*

The authors are with the School of Electrical Engineering, China University of Mining and Technology, Xuzhou 221116, China (e-mail: timelyrainy@163.com; 18260722082@163.com; cumt_yzy1997@163.com; ts21130168p31@cumt.edu.cn; 3465281940@qq.com; 1036759138@qq.com).

Color versions of one or more figures in this article are available at https://doi.org/10.1109/TPEL.2023.3239117.

Digital Object Identifier 10.1109/TPEL.2023.3239117

by analyzing the passive sensing coils induction voltage to achieve MOD function. In addition to the MOD method through passive sensing coils, MOD can also be achieved through active sensing coils. The literature [25] utilizes active sensing coils, and when MOs intrusion causes a detuning of the detection circuit, the output voltage of the detection circuit changes. In the literature [26], a method achieving MOD and DoP functions by analyzing the phase difference of the detection circuit is proposed.

The most current detection methods are based on passive sensing coils. The methods based on passive sensing coils and system parameters mostly generate the excitation magnetic field through the Tx coil, whereas the detection excitation magnetic field has the characteristics of spatial nonuniformity and the existence of passing zero position of magnetic induction intensity. The literature [27] analyzes the problem of uneven spatial magnetic field distribution of the Tx coil leading to the relatively low sensitivity of detection at certain locations, and a multithread sensing coil structure is proposed to achieve relatively uniform induced voltage of MOs at different positions of the sensing coil. In addition, the passing zero position of the magnetic induction of the Tx coil results in a MOD detection blind zone, and the existing research work does not provide a targeted analysis of this detection blind zone problem.

In this article, a bipolar checkerboard MOD technology is proposed to eliminate the detection blind zone caused by the excitation magnetic field in the existing MOD technology of EV wireless charging systems. The causes of the blind zone based on the magnetic field of the Tx coil are analyzed, and the principle of eliminating the blind zone of the bipolar checkerboard MOD system is studied. The detection voltage variation rate of the sensing coil as its sensitivity is defined; then, the relationship between the sensitivity and the number of checkerboard grids, side length, and number of turns is analyzed, and then the size parameters of the bipolar checkerboard sensing coil sets are optimized. A set of MOD system circuit structures is designed, and the design method of circuit parameters is analyzed. The method eliminates the detection blind zone of the excitation magnetic field, the EVs wireless charging system and the MOD system can work independently as well.

II. Analysis of Detection Blind Spot Generated by Excitation Magnetic Field of Tx Coil

A. Blind Spot Generation Mechanism of Tx Coil Excitation Magnetic Field

It is well known that the SAE standard is widely used in the field of wireless charging for EVs. Therefore, this article elaborates on the causes of blind spot generation of excitation magnetic field based on a Tx coil meeting SAE J2954 WPT1 requirements. Fig. 1 shows the dimensional parameters of the Tx coil meeting the requirements of WPT1, with a coil length of 580 mm, the width of 420 mm, the thickness of 93.6 mm, and the number of 15 turns.

Fig. 2 illustrates the magnetic field direction of one long side section of Tx coil. Assuming that the coil is numbered 1–15 from the outside to the inside of the wire, the amplitude of the magnetic field can be calculated by using the Biot–Savart law, and the direction of the magnetic field can be determined using the right-handed rule.

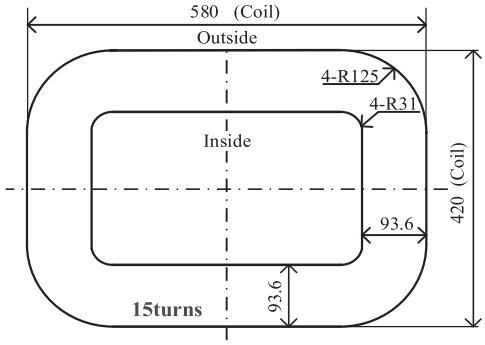

Fig. 1. Tx coil size meeting the requirements of WPT1.

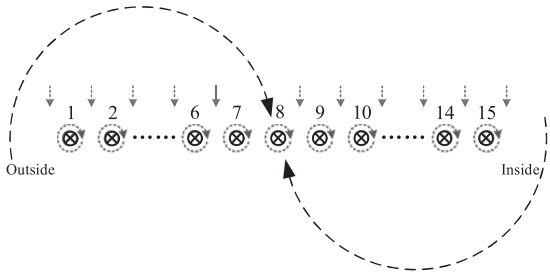

Fig. 2. Schematic diagram of the magnetic field direction of a long-sided section of Tx coil.

Assuming that the current direction of the line is perpendicular inward, the magnetic induction intensity direction of lines 1–7 is directed downward at position 8, and the magnetic induction intensity direction of lines 9–15 is directed upward at position 8. Since the 15 lines have symmetry in position 8, the two magnetic induction intensities are equal in amplitude and opposite in direction. Therefore, the magnetic induction intensity is zero at position 8 for the 15 lines, and the magnetic induction intensity direction is directed downward for the remaining three sides of the Tx coil in that section. So, the magnetic induction intensity passes zero position between lines 1 and 8.

There is a strong eddy current effect of MOs in high-frequency alternating magnetic field. Therefore, an eddy current magnetic field B_{ed} is generated in the opposite direction of the excitation field B_{ex}. Assume that there is a passing zero position of magnetic induction intensity, with the left side of the magnetic field directed upwards and the right side of the magnetic field directed downwards, and the peak magnetic induction intensity of both side is B_{ex}. The peak magnetic induction intensity of eddy currents on the left side of the MO is $B_{\mathrm{ed\_left}}$, and the peak magnetic induction intensity of eddy currents on the right side of the MO is $B_{\mathrm{ed\_right}}$. The angular frequency of the magnetic field is ω. The area of the MO on the left is S_{left}, and the area of the MO on the right is S_{right}. Then, the magnetic flux of the MOD sensing coil changes, and its flux variation is shown in (1)

and (2) as follows:

$$\Delta\phi_{\text{left}} = \sqrt{2}\, B_{\text{ed\_left}} S_{\text{left}} \sin\omega t \tag{1}$$

$$\Delta\phi_{\text{right}} = -\sqrt{2} B_{\text{ed\_right}} S_{\text{right}} \sin\omega t. \tag{2}$$

The voltage variation of the sensing coil is shown in (3) and (4)

$$\begin{aligned}\Delta\, u_{\text{left}} &= N\frac{d}{dt}\Delta\phi_{\text{left}} \\ &= \sqrt{2}\omega N B_{\text{ed\_left}} S_{\text{left}} \sin\left(\omega t + \frac{\pi}{2}\right)\end{aligned} \tag{3}$$

$$\begin{aligned}\Delta\, u_{\text{right}} &= N\frac{d}{dt}\Delta\phi_{\text{right}} \\ &= -\sqrt{2}\omega N B_{\text{ed\_right}} S_{\text{right}} \sin\left(\omega t + \frac{\pi}{2}\right).\end{aligned} \tag{4}$$

When a symmetrical MO center position coincides with the magnetic induction intensity passing zero position, the MO areas S_{left} and S_{right} are equal in size. The magnetic induction intensity of eddy current $B_{\text{ed\_left}}$ and $B_{\text{ed\_right}}$ is equal in amplitude and opposite in direction. The induction voltage is one positive and one negative, as shown in (5), and the value of voltage change Δu of the sensing coil can be found to be equal to 0. Therefore, this position is a blind spot. But due to the presence of eddy currents, energy transfer is impeded and MOs are heated up. So, it is also essential to detect MOs in this blind spot

$$\Delta u = \Delta u_{\text{left}} + \Delta u_{\text{right}} = 0. \tag{5}$$

Since the MOD excitation field is not completely symmetrical on both sides of the zero position of the uniform magnetic field, the probability of asymmetric shape of metal foreign objects is higher. Therefore, the detection blind spot is located near the excitation magnetic field passing zero position.

B. Simulation Analysis of Magnetic Induction Intensity of Tx Coil Passing Zero Position and Blind Spot Position

Since the MOD function mainly relies on the *Z*-axis magnetic field of the excitation field, to find the location of the magnetic induction intensity B_z passing zero in the *Z*-axis direction of the Tx coil magnetic field, the simulation model of Tx coil meeting the requirements of SAE J2954 WPT1 is built by COMSOL simulation software. The distribution of magnetic induction intensity B_z along the *Z*-axis direction on the surface of Tx coil is shown in Fig. 3 when the coil current is set at 10 A.

It can be seen from Fig. 3 that the magnetic induction intensity passing zero position on the central axis of its long side locates at 172 mm. And at the corner of the coil, the magnetic induction intensity passing zero position is closer to the outer boundary.

The method that compares the change in voltage before and after the intrusion of MOs is called the voltage variation MOD; the method that uses symmetrical multiple sensing coils to offset the induction voltages is called the voltage difference MOD. The voltage variation MOD requires a constant current in the Tx coil. The EV wireless charging standards SAE J2954 and GB/T 38775 both use *LCC–LCC* resonant circuits, which theoretically guarantee a constant Tx coil current. However, the current of the Tx coil will fluctuate in engineering, so this method is not reliable.

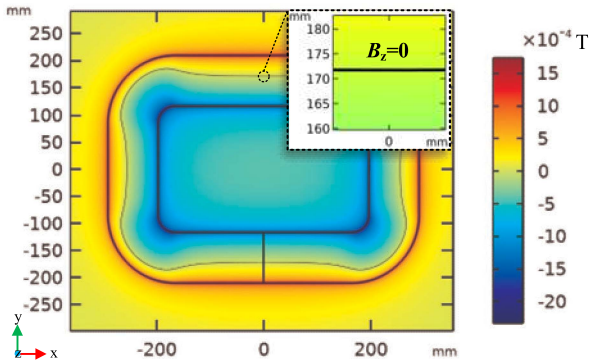

Fig. 3. Distribution of magnetic induction intensity B_z along the *Z*-axis on the surface of Tx coil.

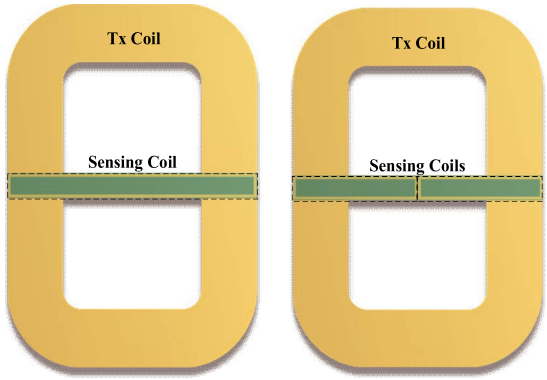

Fig. 4. Schematic diagram of voltage variation and difference MOD device. (a) Voltage variation MOD. (b) Voltage difference MOD.

As shown in Fig. 4, sensing coils of voltage variation MOD and voltage differential MOD are added on the Tx coil simulation model. The turns of the sensing coils are 5 and the width is 40 mm. The length of voltage variation sensing coils is 420 mm, and the length of voltage difference sensing coils is 210 mm. An aluminum cylindrical MO with the diameter of 25 mm and the thickness of 2 mm moves along the central axis. The electrical conductivity of aluminum is 3.774×10^7 S/m; the relative magnetic permeability is 1; and the relative dielectric constant is 1.

Fig. 5 shows the trend of the sensing coil induction voltage variation during the movement of the MO along the central axis of the long edge.

As can be seen from Fig. 5, there are two blind spots in the voltage variation MOD technique, which are the magnetic field blind spot and the boundary blind spot. There is an additional one central blind spot for the voltage difference MOD technique. The simulation results show that both detection methods produce two magnetic field blind spots near 172 mm, which is just the location of magnetic induction intensity passing zero on the central axis.

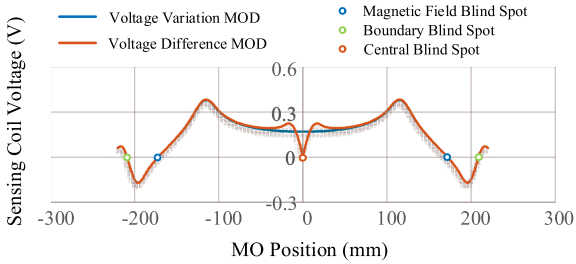

Fig. 5. Sensing coil induction voltage variation curve with MO position.

III. Principle of Bipolar Checkerboard MOD System

A. Structure of Bipolar Checkerboard MOD System

The schematic diagram of the bipolar checkerboard MOD system is shown in Fig. 6, which includes two parts: the EV wireless charging system and the MOD system. EV wireless charging system operating frequency $f_2 = 85$ kHz, MOD system operating frequency $f_1 = 8.5$ kHz, and the two systems can work independently of each other.

The EV wireless charging system includes inverter, Tx coil, Rx coil, EV, etc.

The MOD system includes three parts: bipolar checkerboard sensing coil sets, excitation coil circuit, and sensing coil circuit.

1) The bipolar checkerboard sensing coil sets consist of two parts: MOD excitation coil and MOD sensing coils. The excitation coil is placed above the Tx coil and can generate the excitation magnetic field B_z, which is the opposite direction of the adjacent checkerboard grid. The sensing coils are placed above the excitation coil to eliminate the blind zone caused by the excitation magnetic field.
2) The excitation coil circuit consists of a signal generator, a power amplifier, and a passive filter circuit: the signal generator generates an 8.5 kHz sine wave signal source; the power amplifier amplifies the signal and provides the excitation power supply for the excitation coil; inductive L_1 and capacitors C_1 of the passive filter circuit reduce the induced current content generated in the excitation coil by the 85 kHz energy transfer magnetic field.
3) The sensing coil circuit includes four parts: active low-pass filter (LPF), rectifier circuit, zero adjustment circuit, and voltage differential circuit. The active LPF is directly connected to the sensing coil and is used to filter out the 85 kHz detection voltage signal. The rectifier circuit converts the ac voltage signal to dc voltage signal U_o. The voltage differential circuit makes the difference between the dc voltage signal U_o and the standard reference voltage signal U_{ref}, and adjusts the sliding resistor to ensure that the detection voltage ΔU is zero in no MOs situation.

Both the MOD excitation and sensing coils of the bipolar checkerboard sensing coil sets are made by printed circuit board (PCB) board, and the PCB layout method is described as follows.

1) Excitation coil structure: The excitation coil can generate a bipolar checkerboard grid excitation magnetic field. Adjacent coils of the bipolar checkerboard excitation coil are routed in opposite directions, and the currents of adjacent coils are also in opposite directions. Thus, the magnetic field of the adjacent coils is in opposite directions and the boundary of the adjacent coils is the position where the magnetic induction intensity passes zero. Fig. 7 shows the PCB routing diagram of the bipolar checkerboard excitation coil.

In Fig. 7, the red line is the top layer; the blue is the bottom layer; the whole excitation coil is wound by a single line; the line width is 2 mm; the number of checkerboard grids is $M \times N$; and the side length of checkerboard grids is l.

2) Sensing coil structure: In order to eliminate the blind zone caused by the excitation magnetic field; the sensing coil adopts the bipolar coil winding method. The winding direction of the sensing coil is reversed once at each position where the magnetic induction intensity of the excitation coil passes zero. Due to the reversal of the winding direction of the sensing coil, the negative induced voltage generated by the reversed magnetic field on the sensing coil becomes positive induced voltage, thus eliminating the blind zone caused by the excitation magnetic field. Fig. 8 shows the PCB routing diagram of the sensing coil.

In Fig. 8, the red line is the top layer; the blue is the bottom layer; it is an entire sensing coil connected at the top layer to the bottom layer by vias; the whole sensing coil is a multiturn coil; the line width is 0.5 mm; the line spacing is 0.5 mm; the number of checkerboard grid is M; and the side length of the checkerboard grid is l.

B. Principle of Independent Work of MOD System and EV Wireless Charging System

The EV wireless charging system uses a unipolar magnetic circuit mechanism, and the MOD system uses a bipolar magnetic circuit mechanism. The coupling between the two systems is low under the condition of no MOs, whereas the invasion of MOs will increase the coupling between the two systems. Since the magnetic field intensity of the EV wireless charging system is much higher than that of the MOD system, the influence of the EV wireless charging system on the MOD system is much stronger than the influence of the MOD system on the EV wireless charging system.

As shown in Fig. 9, to ensure independent work between the two systems, the operating frequency of the MOD system is selected as 8.5 kHz. *LC* passive filter circuit is added in front of the excitation coil to improve the quality factor of the circuit, thus reducing the 85 kHz induced current content from the EV wireless charging system. The detection circuit uses an active LPF to process the detection voltage from the sensing coil, filtering out the 85 kHz induced voltage generated by the magnetic field of the EV wireless charging system on the sensing coil. Then, the ac voltage signal is converted to a dc voltage signal through a rectifier circuit.

This MOD system achieves independent work in two aspects: the coil structure and the circuit structure.

1) Coil structure: The MOD coil sets use a bipolar structure and the Rx coil and Tx coil use a unipolar structure. Although the excitation coil changes the magnetic geometry of the

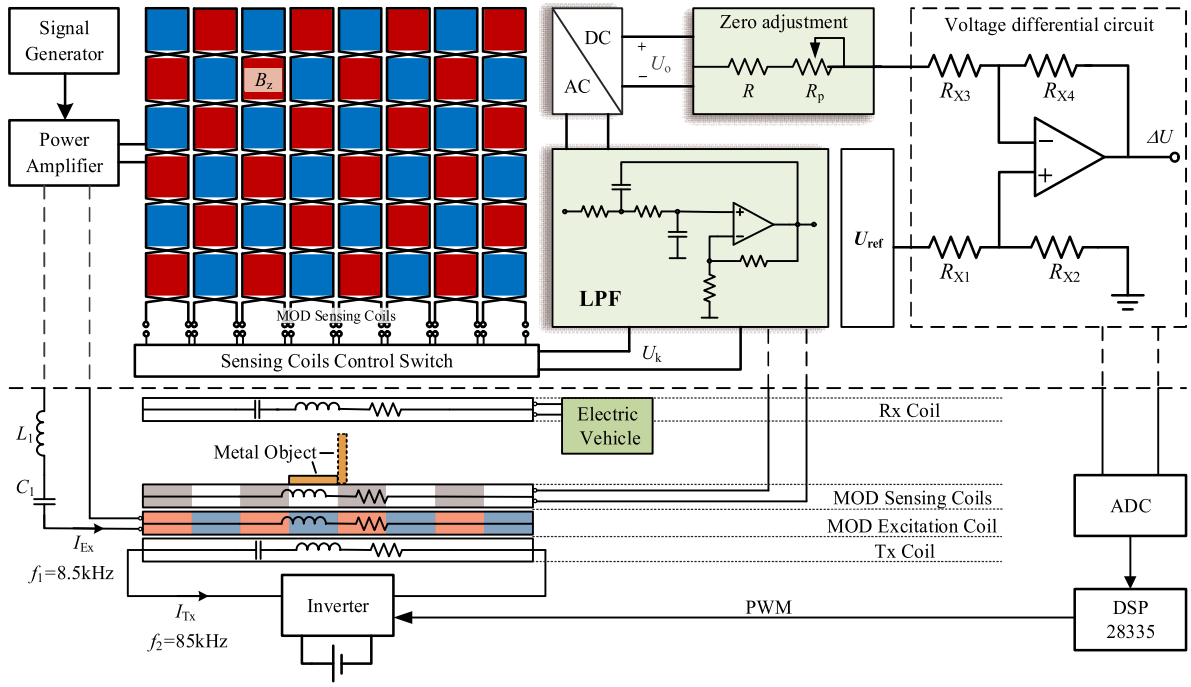

Fig. 6. Schematic diagram of bipolar checkerboard MOD system.

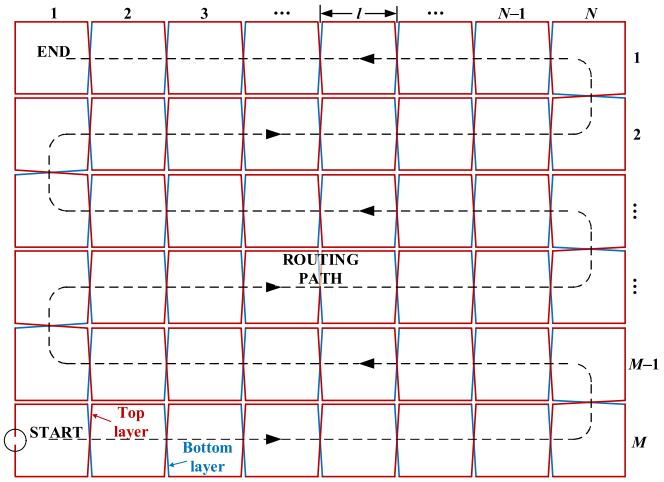

Fig. 7. PCB routing diagram of bipolar checkerboard excitation coil.

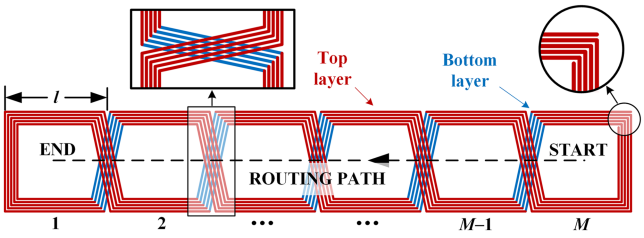

Fig. 8. PCB routing diagram of sensing coil.

EV wireless charging system, the MOD coil sets are fully decoupled from the Rx coil and Tx coil in magnetic circuit. So, there is a lower coupling coefficient between the MOD

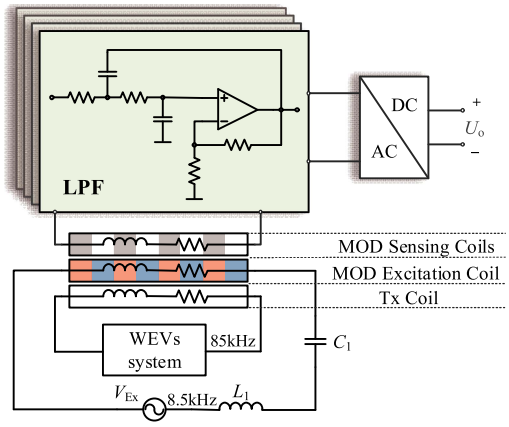

Fig. 9. Schematic diagram of the independent work of MOD system and EV wireless charging system.

system and the EV Wireless Charging System in the absence of MO.

2) Circuit structure: Optimizing the design of the *LC* passive filter and LPF circuit parameters by considering the coupling coefficient between the Tx coil and the excitation coil. Thus, reducing the mutual influence between the two systems. It makes the MOD signal more stable and reduces the losses caused by the deployment of MOD coil sets between Rx coil and Tx coil.

After parameter optimization, the influence of the Tx Pad on the MOD system becomes lower. The Rx Pad influence on the MOD system will be even smaller for the lower coupling coefficient of the Rx Pad and the MOD coil sets.

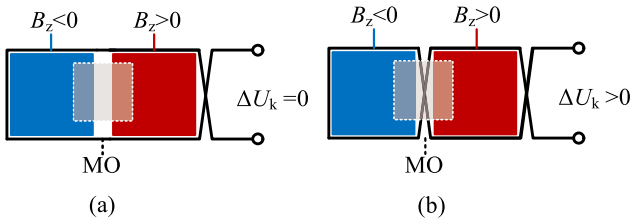

Fig. 10. Bipolar sensing coil blind zone elimination schematic. (a) Unipolar. (b) Bipolar.

C. Principle of Eliminating Detection Blind Zone Caused by Excitation Magnetic Field

The schematic diagram for eliminating the blind zone by the bipolar sensing coil is shown in Fig. 10. The sensing coil in Fig. 10(a) uses a unipolar coil winding method and the sensing coil in Fig. 10(b) uses a bipolar coil winding method.

A MOD excitation magnetic field with magnetic induction intensity passing zero position exists. For the unipolar sensing coil in Fig. 10(a), when the MO is located in the blind spot position of the magnetic field, the induced voltage variation $\Delta U_k = 0$ of the sensing coil before and after the MO invasion. For the bipolar sensing coil in Fig. 10(b), wound once in the passing zero position in reverse, the induced voltage variation $\Delta U_k > 0$ of the bipolar sensing coil, thus eliminating the detection blind zone caused by the excitation magnetic field.

According to the results of the previous analysis, the detection blind zone caused by the excitation magnetic field is the reason of using Tx coil as the MOD excitation source. Its magnetic induction intensity has passing zero position, and the passing zero position is irregular in shape. The bipolar checkerboard MOD excitation coil can generate a fixed passing zero position and combined with the bipolar sensing coils of the same checkerboard grid side length can eliminate the detection blind zone caused by the excitation magnetic field.

A bipolar checkerboard excitation coil model is built using COMSOL, and the peak excitation current is set to 1 A. Fig. 11 shows the magnetic induction intensity B_z distribution along the z-axis direction on the surface and at the tangent position of the excitation coil. Fig. 12 shows the schematic diagram of magnetic induction lines at the tangent position of the excitation coil. The direction of the magnetic induction intensity of adjacent coils is opposite, and the boundary between adjacent coils is the position where the magnetic induction intensity passing zero.

As shown in Fig. 12, the bipolar checkerboard excitation coil is used to generate the excitation magnetic field, which has a longitudinal magnetic field along the z-axis and a transverse magnetic field along the x-axis. Thus, this detection method has both transverse and longitudinal detection capabilities for MOs, similar to the longitudinal MO detection principle mentioned in the literature [25].

D. Principle of MOD Judgment

Since MOs are judged by the difference of the detection voltage, the amplitude of the detection voltage signal U_o is not zero in the absence of MOs, and direct acquisition of the detection voltage signal reduces the range of judgment for MOs. Therefore, the voltage difference circuit is used to further process the detection voltage signal. Fig. 13 shows the MOD judgment circuit diagram.

The detection voltage U_o is adjusted by a sliding resistor R_p and differenced with a reference voltage U_{ref}. This circuit has a certain amplification of the differential voltage, which is related to the value of the resistor in the circuit. Therefore, the amplification varies with the sliding resistor. The differential circuit output voltage signal ΔU is guaranteed to be zero in the absence of MOs. When ΔU is not zero, it represents the invasion of MOs.

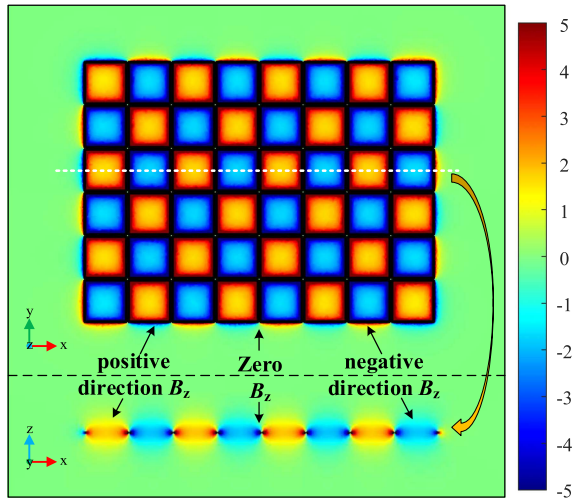

Fig. 11. Distribution of magnetic induction intensity B_z on the surface and at the tangent position of the bipolar checkerboard excitation coil.

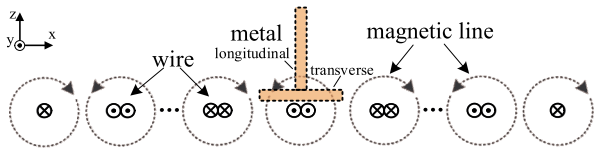

Fig. 12. Schematic diagram of the magnetic induction lines at the tangent position of the bipolar checkerboard excitation coil.

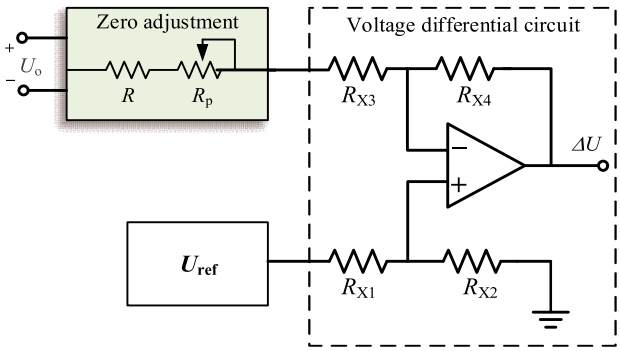

Fig. 13. Circuit diagram of MOD judgment.

Due to the errors and temperature drift of the devices in the hardware circuit, the voltage signal ΔU is not guaranteed to be zero in the absence of MOs during the operation of the MOD circuit. For this reason, it is necessary to set a suitable voltage threshold V_{th}, and then the MOD judgment condition is

$$\Delta U < -V_{\text{th}} \text{ or } \Delta U > V_{\text{th}}. \tag{6}$$

IV. Parameters Design of MOD Coil Sets and Circuit

A. Definition of MOD Sensitivity

In order to visually evaluate the detection capability of the sensing coil sets, this article uses the definition method of sensitivity in the literature [22] and the detection sensitivity is defined in the following equation:

$$S = \frac{|U_{\text{k}} - U'_{\text{k}}|}{U_{\text{k}}} \times 100\% = \frac{\Delta U_{\text{k}}}{U_{\text{k}}} \times 100\%. \tag{7}$$

The peak-induced voltage of the sensing coil is U_{k} when there is no MO. The peak induced voltage of the sensing coil is U'_{k} when the MOs are invaded. The difference in the induced voltage change of the sensing coil is ΔU_{k}, and the rate of induced voltage change is defined as the sensitivity S.

The sensitivity is used as the evaluation index for the parameter design of the sensing coil sets. The parameters include the checkerboard grid side length and the number of turns of the excitation and sensing coils.

B. Size Parameters Design of Excitation Coil

For highly sensitive smaller MOs, the size of the sensing coils needs to be reduced. However, this article focuses on the causes and solutions of the detection blind spot of the excitation magnetic field, and the bipolar checkerboard MOD method can effectively eliminate the blind spot from the structure. Therefore, a square aluminum plate with a side length of 80 mm and a thickness of 1 mm is used as a MO for the analysis parameters.

In order to cover the entire Tx coil area, the excitation coil and sensing coil size should be slightly larger than the size of the Tx coil, thus satisfying the following conditions:

$$\begin{cases} Nl > 580 \text{ mm} \\ Ml > 420 \text{ mm}. \end{cases} \tag{8}$$

To ensure that the coupling coefficient between the sensing coil sets and the Tx coil is as low as possible in the absence of MOs, the number of checkerboard grid N and M of the bipolar checkerboard sensing coil sets should be an even number. Fig. 14 shows the relationship between the number of checkerboard grid $M \times N$ and the length of the checkerboard grid l. As the length l increases, the number $M \times N$ is decreasing, and the number of induction voltages of the sensing coils that need to be sampled is also decreasing. Therefore, the number $M \times N$ should be as small as possible while meeting the sensitivity requirements.

In this article, it is analyzed using a square aluminum plate with a side length of 80 mm and a thickness of 1 mm as a MO. When the MO is present, a simulation model is built by COMSOL to analyze the sensitivity with different checkerboard side lengths. The sensing coil size is related to the excitation coil size, and the sensitivity analysis using (7). As the excitation coil is an active coil, its equivalent ac resistance is high. In order to reduce the power loss, the turns of the excitation coil are set to 1. Fig. 15 shows the variation of sensitivity for different checkerboard grid side lengths.

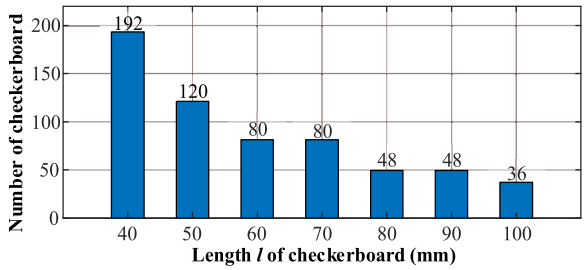

Fig. 14. Graph of the relationship between the number $M \times N$ and the side length l.

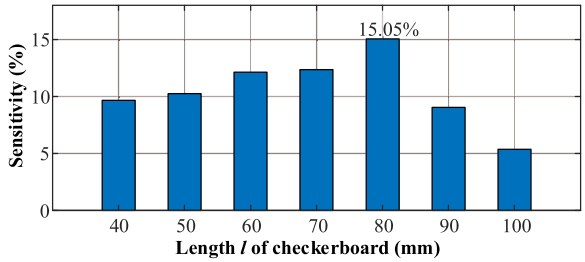

Fig. 15. Graph of the variation of detection sensitivity with the side length l (the turns of sensing coil is 5).

From Fig. 15, it can be seen that the detection sensitivity is highest when the side length of the checkerboard grid is equal to the side length of the MO. Therefore, the side length of the checkerboard grid of the excitation coil is set to 80 mm, and the number of checkerboard grids is 6×8.

C. Size Parameters Design of Sensing Coil

The number and side length of the checkerboard grid of the sensing coil should be consistent with that of the excitation coil. When the excitation coil size is determined, the side length of the checkerboard grid is set to 80 mm and the number of checkerboard grids is 6×8. The turns of the sensing coil is the only variable that can be optimized. Using COMSOL simulation software is used to analyze the MOD sensitivity for different turns of the sensing coil. Fig. 16 shows the variation of sensitivity with the turns of the sensing coil for the checkerboard grid with 80 mm side length.

As can be seen from Fig. 16, the growth rate of sensitivity decreases as the number of turns increases. To ensure that the sensitivity can be maintained at about 15%, the turns of the sensing coil is finally set to five turns, and the sensitivity under this parameter is 15.05%.

Table I shows the parameters of the bipolar checkerboard excitation coil and sensing coil, with the self-inductance and internal resistance being the actual measured data of the PCB coil.

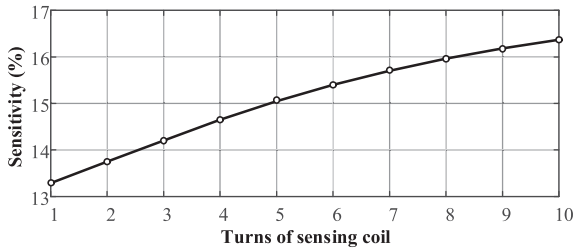

Fig. 16. Variation curve of detection sensitivity with the turns of sensing coil ($l = 80$ mm).

TABLE I
DESIGN PARAMETERS OF MOD COIL SETS

Parameter	Excitation coil	Sensing coil
Side length of the checkerboard grid l	80 mm	80 mm
Number of checkerboard grid $M\times N$	6×8	1×8
Turns	1	5
Self-inductance	16.6 μH	38.4 μH
Internal resistance (8.5 kHz)	3.62 Ω	6.19 Ω

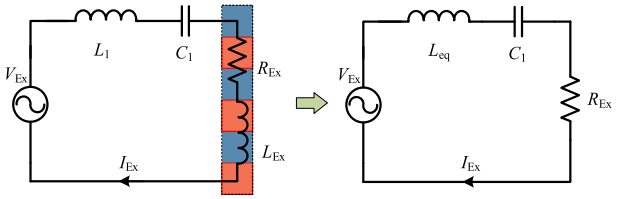

Fig. 17. Excitation coil passive filter circuit diagram.

D. Parameter Optimization of Excitation Coil Passive Filter Circuit

The excitation coil passive filter circuit and its equivalent circuit are shown in Fig. 17.

In which, the peak input voltage of the excitation coil passive filter circuit is V_{Ex}; the characteristic angular frequency is ω_c; the inductance of the *LC* filter circuit is L_1; the capacitance is C_1; the inductance of the excitation coil is L_{Ex}; the resistance of the excitation coil is R_{Ex}; and the current of the excitation coil is I_{Ex}.

Inductor L_1 of the *LC* filter circuit is designed according to the integer multiple n of the excitation coil inductance L_{Ex}, and then the relationship of each circuit parameter satisfies (9)–(11)

$$L_{eq} = L_1 + L_{Ex} = nL_{Ex} \tag{9}$$

$$\omega_c = \frac{1}{\sqrt{L_{eq}C_1}} \tag{10}$$

$$V_{Ex} = \left(j\omega L_{eq} + \frac{1}{j\omega C_1} + R_{Ex}\right) I_{Ex}. \tag{11}$$

Accordingly, the following can be found.

The voltage division V_R of the resistor R_{Ex} is

$$V_R = R_{Ex} I_{Ex}. \tag{12}$$

The expression of the transfer function of the circuit is

$$A(s) = \frac{s}{\frac{L_{eq}}{R_{Ex}}s^2 + s + \frac{\omega_c^2 L_{eq}}{R_{Ex}}}. \tag{13}$$

Quality factor Q_1 of the circuit is

$$Q_1 = \frac{\omega L_{eq}}{R_{Ex}}. \tag{14}$$

The amplitude and frequency response of the circuit is expressed as

$$20\lg|A(j\omega)| = 20\lg\frac{1}{\sqrt{1+Q_1^2\left(1-\frac{\omega_c^2}{\omega^2}\right)^2}}. \tag{15}$$

In order to ensure independent work between the EV wireless charging system and the MOD system with a high detection accuracy, Q_1 should be increased as high as possible. The total harmonic distortion (THD) of the excitation current is used to evaluate the independent working capability, and the equivalent calculation formula for THD is

$$\text{THD} = \frac{\sqrt{I_2^2 + I_3^2 + I_4^2 + \cdots + I_n^2}}{I_1} \tag{16}$$

where I_1 is the excitation current I_{Ex} and I_n (n = 2,3,4, …) is the induced current of other frequencies.

When there is a square aluminum MO of size 80 × 80 × 1 mm^3 on the sensing coil, the mutual inductance between the Tx coil and the excitation coil is about 0.3 μH. Setting the peak value of current I_{Tx} in the Tx coil to 10 A, thus the peak value of induced voltage V_2 in the excitation coil is 1.6 V. When the peak value of excitation current I_{Ex} is set to 1 A, in order to obtain high detection accuracy, and the current in the excitation coil has good sinusoidal characteristics, the THD value is limited to be less than 1%. Thus, the peak induction current I_2 in the excitation coil should be less than 0.01 A. Substitute the induced voltage V_2 and induced current I_2 into the following equation:

$$I_2 = \frac{V_2}{j\omega nL_{Ex} + \frac{1}{j\omega C_1} + R_{Ex}}. \tag{17}$$

It can be calculated that n is greater than 18.24; therefore, $n = 20$ is chosen for the experimental design. To more visually analyze the attenuation degree of the induced current, the amplitude-frequency characteristic curves of the excitation circuit for $n = 1$ and 20 are plotted using (15), as shown in Fig. 18.

As can be seen in Fig. 18, the attenuation of the excitation coil circuit for the 85 kHz signal increases from 8.37 to 33.72 dB. Therefore, the excitation coil circuit with the addition of *LC* passive filtering has an enhanced degree of attenuation for the 85 kHz energy transfer magnetic field.

For a more visual analysis of the degree of independent work between the two circuits, the fast Fourier transform (FFT) of the excitation coil current is analyzed. Fig. 19 shows the FFT spectrum analysis of the excitation coil current.

From Fig. 19, it can be seen that the THD value is 0.93%, which meets the design requirement of less than 1%. Thus, there is a good independent working ability between the excitation coil circuit and the Tx coil circuit.

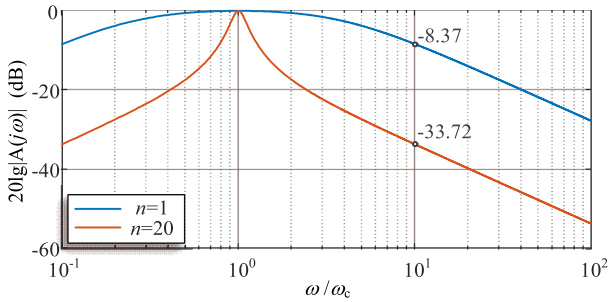

Fig. 18. Amplitude-frequency characteristic curve of excitation coil circuit.

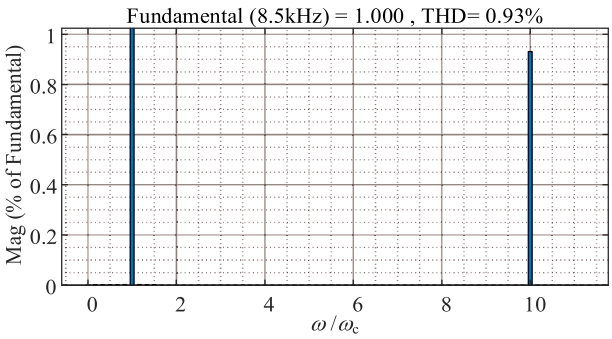

Fig. 19. FFT spectrum analysis of the excitation coil current.

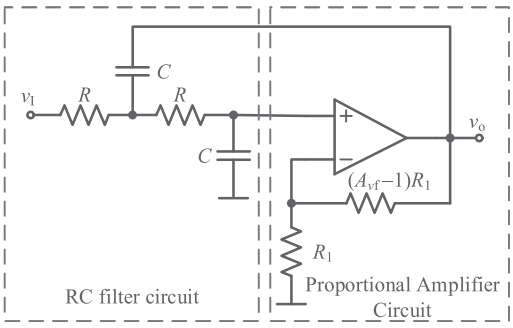

Fig. 20. Second-order active LPF circuit diagram.

E. Parameter Optimization of Sensing Coil Active LPF Circuit

The sensing coil circuit has a high output impedance, and its circuit quality factor is low. The passive filter circuit cannot effectively filter out the interference of the EV wireless charging system on the detection voltage signal of the sensing coil; therefore, the second-order active LPF circuit is used to process the detection voltage signal. Fig. 20 shows the diagram of the second-order active LPF circuit.

The second-order active LPF circuit satisfies (18)–(20)

$$\omega_c = \frac{1}{RC} \tag{18}$$

$$Q_2 = \frac{1}{3 - A_{vf}} \tag{19}$$

$$A_0 = A_{vf} \tag{20}$$

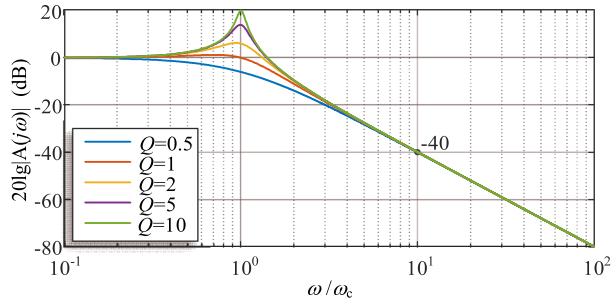

Fig. 21. Second-order active LPF amplitude-frequency characteristic curve.

TABLE II
DESIGN PARAMETERS OF MOD CIRCUIT

Parameter	Value	Unit
L_{EX}	16.6	μH
L_1	315.4	μH
C_1	1	μF
C	10	nF
R	1.87	kΩ
n	20	Turns

where ω_c is the characteristic angular frequency; Q_2 is the equivalent quality factor; A_0 is the passband voltage gain of the LPF; and A_{vf} is the voltage gain of the in-phase proportional amplifier circuit.

The transfer function expression of the second-order LPF circuit is

$$A(s) = \frac{A_0 w_c^2}{s^2 + \frac{w_c}{Q_2} s + w_c^2}. \tag{21}$$

The amplitude-frequency response expression of the second-order LPF circuit is

$$20\lg|A(j\omega)| = 20\lg \frac{1}{\sqrt{\left[1 - \left(\frac{\omega}{\omega_c}\right)^2\right]^2 + \left(\frac{\omega}{\omega_c Q_2}\right)^2}}. \tag{22}$$

As shown in Fig. 21, the amplitude-frequency characteristic curve of the second-order LPF can be plotted by (22).

As can be seen from Fig. 21, the correlation is not significant between the attenuation degree of the 85 kHz signal and the equivalent quality factor Q. Choosing a quality factor of 1, its attenuation of the 8.5 kHz signal is 0 dB, and the voltage gain of the circuit A_0 is 2. To achieve independent work of the detection system with higher detection accuracy, the detection circuit uses a multistage second-order LPF connected in series.

Table II shows the circuit parameters of the passive filter circuit and the second-order active LPF circuit.

The MOD system is parametrically designed for an 80 mm large aluminum plate. In this case, the coupling coefficient between the excitation coil and the Tx coil is 0.3 μH. If the MO is smaller, the coupling coefficient will be smaller. The designed parameters are suitable for smaller MOs. If the MO is larger, the coupling coefficient will be higher. Although this will increase the interaction between the two systems, larger size MOs are more easily detected. The EV wireless charging

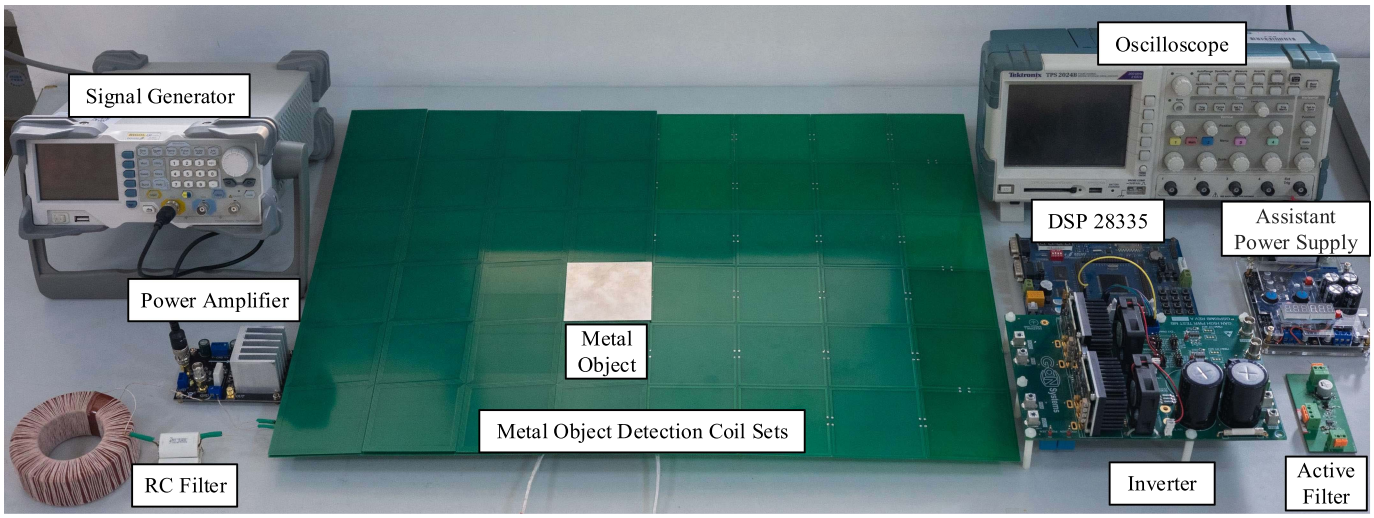

Fig. 22. Bipolar checkerboard MOD experimental circuit diagram.

system is stopped immediately when a MO is detected, so there is no need to be concerned about the interaction between the two systems.

V. Experimental Verification of MOD System

A bipolar checkerboard MOD experimental platform is built, and Fig. 22 shows the experimental circuit diagram. The inverter is supplied with an 85 kHz pulsewidth modulation signal using DSP28335. The power amplifier is supplied with an 8.5 kHz sine wave signal using a signal generator. The Rx coil is compensated by *LCC* resonance. Tx coil current is controlled by adjusting the inverter dc input voltage. The excitation coil current is controlled by adjusting the signal generator input voltage. To ensure higher detection accuracy, the sensing coil circuit is designed with a four-stage second-order active LPF circuit. It can attenuate the voltage signal of 85 kHz to 1.6×10^{-9} times of the original and can increase the voltage signal of 8.5 kHz to 16 times of the original.

In the experiments, the distance between the Tx and Rx coils of the EV wireless charging system is 15 cm. Tx coil current peak is 10 A. Rx coil current peak is 13 A. Output power is 710 W and the efficiency is 87.1%.

Fig. 23 shows the structure of the MOD coil sets, with the excitation coil and sensing coil stacked on top of the Tx coil in turn. The Tx coil is on the bottom layer, the excitation coil is on the middle layer and the sensing coil is on the top layer. Moreover, the excitation and sensing coils are actually spread over the entire Tx coil.

The MO is placed at different positions on the sensing coil during the experiment, and Fig. 24 shows the schematic diagram of the placement of the MO.

In which, m represents the number of rows of the square; n represents the number of columns of the square; and m' represents the adjacent boundary of the two squares.

The square aluminum MO is placed directly above the square P(m,n), in the middle of the two squares P(m',n), and vertically on the adjacent boundary of the two squares P'(m',n).

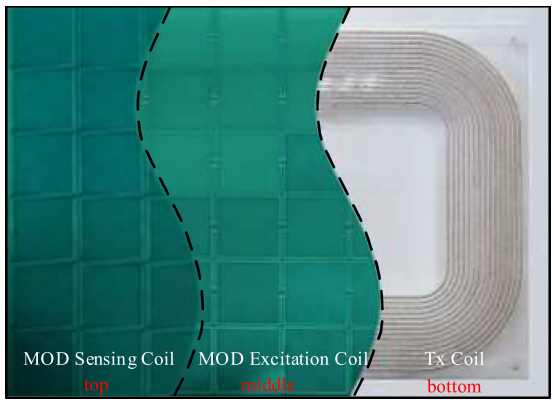

Fig. 23. MOD coil sets structure diagram.

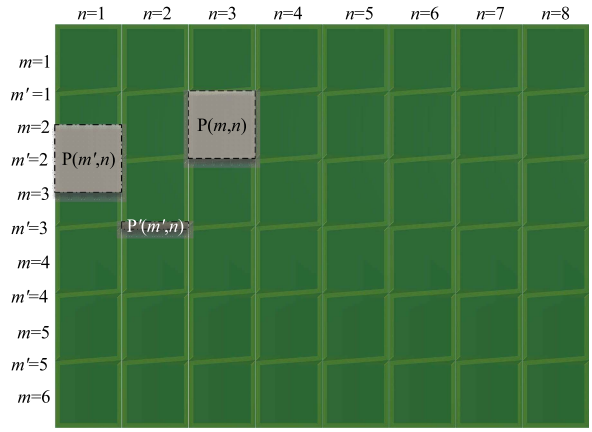

Fig. 24. Schematic diagram of the placement of MOs.

A. Verification of Independent Work

The MO used in the experiment is a square aluminum plate with a side length of 80 mm and a thickness of 1 mm. The metal aluminum plate is placed at position P(3,4) to simulate the

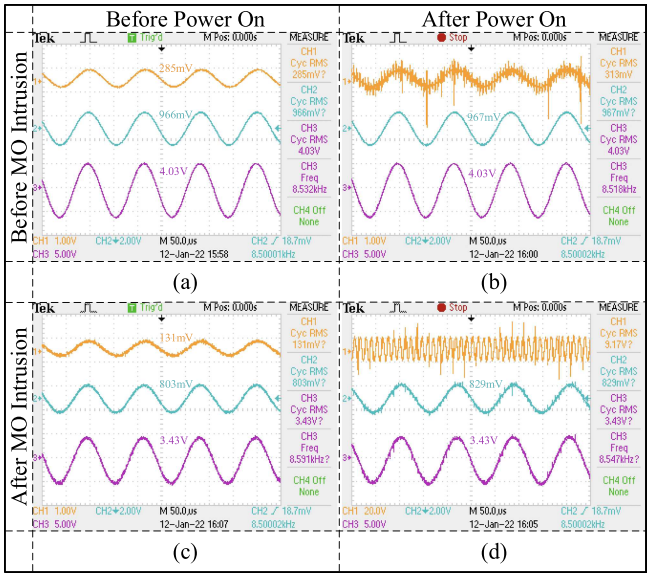

Fig. 25. Detection voltage waveforms with/without MO before and after EV wireless charging system is powered on.

MO intrusion. Fig. 25 shows the detection voltage waveforms with/without MO before and after EV wireless charging system is powered ON. CH1 is the voltage signal waveform of the sensing coil; CH2 is the voltage waveform after the first two stages of filtering; and CH3 is the voltage waveform after four stages of filtering.

Comparing Fig. 25(a) and (c), before the EV wireless charging system is powered ON, the intrusion of MOs leads to the reduction of voltage signal amplitude; comparing Fig. 25(b) and (d), in addition to the reduction of voltage signal amplitude after the EV wireless charging system is powered ON, high-frequency electromagnetic field interference of the energy transfer system is also introduced; comparing Fig. 25(a) and (b), a certain signal interference exists before the MO invasion because of the asymmetry in engineering design of the Tx coil and the sensing coil; comparing Fig. 25(c) and (d), the four-stage active LPF circuit can effectively filter out the high-frequency signal, and the voltage amplitude of CH3 before and after power on is equal. Before the MO invasion, the effective value of CH3 detection voltage before and after power on is 4.03 V; after the MO invasion, the effective value of CH3 detection voltage before and after power on is 3.43 V.

To more visually check the independent working capability of the system, Fig. 26 shows the waveform diagram of the EV wireless charging system power-on and MO intrusion experiment. CH1 is the current I_{Ex} waveform of the excitation coil; CH2 is the current I_{Tx} waveform of the Tx coil; CH3 is the dc output voltage U_{o} waveform of the detection circuit.

The amplitude of the excitation coil current is kept constant at 1 A with/without MO before and after EV wireless charging system is powered ON. The amplitude of the Tx coil current is kept constant at 10 A after power on. Since U_{o} is obtained by uncontrolled rectification of the CH3 voltage waveform in

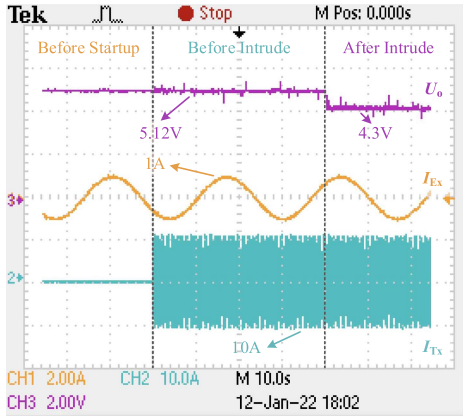

Fig. 26. Waveform diagram of EV wireless charging system power-on and MO intrusion experiment.

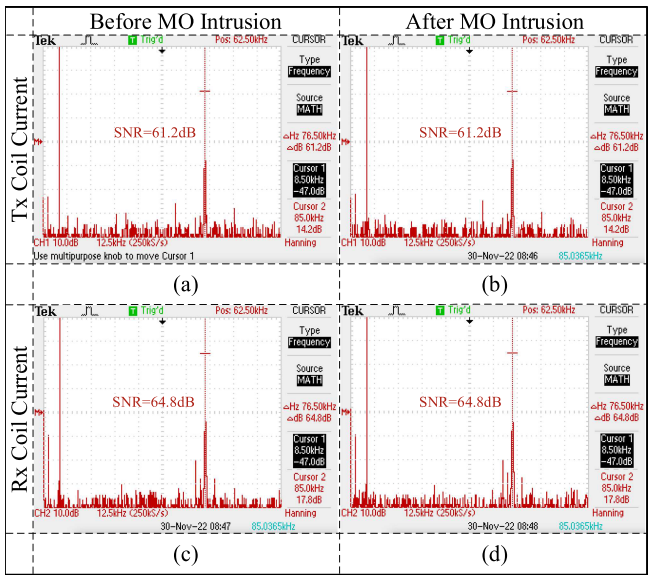

Fig. 27. Spectrum of the currents in the Tx and Rx coils with/without MO.

Fig. 25, and there is a forward voltage drop in the rectifier diode, so the value of U_{o} is slightly lower than the peak voltage before rectification. The dc detection voltage remains constant at 5.12 V before and after power on, and the detection voltage decreases to 4.3 V after the invasion of MO. The experiment proves that the circuit parameters designed in this article effectively realize the independent work between MOD system and EV wireless charging system.

For more visual analyze the effect of the excitation coil current on the Tx and Rx coils current, an FFT analysis of the currents in the Tx and Rx coils was performed. Fig. 27 shows the spectrum of the currents in the Tx and Rx coils with/without MO.

In Fig. 27, the two cursors are tuned to 8.5 and 85 kHz frequencies. An oscilloscope is used to measure the signal-to-noise ratio (SNR) between the two frequencies. The SNR in Tx coil current is 61.2 dB with/without MO. The SNR in Rx coil current is 64.8 dB with/without MO. The SNR values show that the 8.5

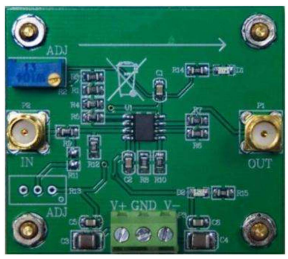

Fig. 28. Experimental device of the zero adjustment and voltage differential circuits.

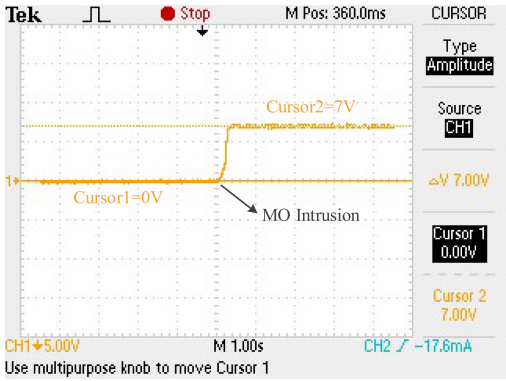

Fig. 29. Variation of the detection voltage ΔU [when an 80 × 80 mm^2 aluminum plate is placed in position P(3, 4)].

kHz current disturbance in the Tx and Rx coils current is very low.

Fig. 28 shows the experimental device of the zero adjustment and voltage differential circuits. By adjusting the resistance of the sliding resistor, the detection voltage ΔU is zero when there is no MO.

Fig. 29 shows the variation of the detection voltage ΔU when an 80 × 80 mm^2 aluminum plate is placed in position P(3, 4). The detection voltage is around zero when there is no MO. The detection voltage changes to 7 V after the intrusion of the MO.

B. Verification of Blind Zone Elimination and Detection Sensitivity

In the absence of MO intrusion, keep the MOD system working continuously; after 5 min of work, there is a 10 mV offset in the detection voltage U_o. After the zero adjustment and voltage differential circuits, the detection voltage offset is expanded to 110 mV. Thus, set the detection voltage threshold V_{th} to ±110 mV, when the detection voltage variation ΔU is greater than $|V_{th}|$, all MOs can be detected.

The sensitivity of the MOD system is analyzed by measuring the detection voltage using different materials and sizes of MOs. Fig. 30 shows different materials and sizes of MOs. All the MOs are 1 mm thick.

Table III shows the detection voltage ΔU for MOs of different materials and sizes. From the analysis of the detection voltage, it can be concluded that copper is easier to detect than aluminum. As the MOD system is designed for an 80 × 80 mm^2 aluminum

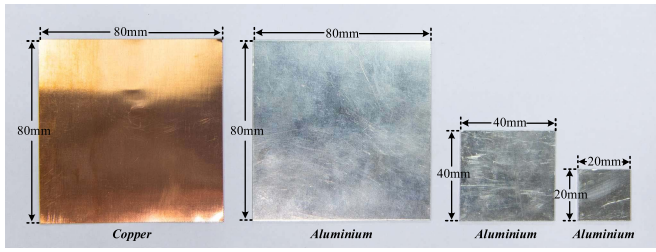

Fig. 30. Different materials and sizes of MOs.

TABLE III
DETECTION VOLTAGE ΔU FOR DIFFERENT MOS

Material	Size	Detection voltage ΔU	Unit
Copper	80×80×1 mm^3	7.94	V
Aluminum	80×80×1 mm^3	7.01	V
Aluminum	40×40×1 mm^3	1.31	V
Aluminum	20×20×1 mm^3	320	mV

plate, it is not sensitive to a 20 × 20 mm^2 aluminum plate. However, it can still be detected when the 20 × 20 mm^2 aluminum plate is placed in some positions on the sensing coil.

To verify that the bipolar checkerboard MOD system can eliminate the detection blind zone caused by the excitation magnetic field and analyze the detection sensitivity of different positions, the MO is placed at different positions of the sensing coils. Fig. 31 shows the histogram of the dc detection voltage variation value ΔU for the MO placed at different positions. The detection sensitivity S is proportional to the voltage variation value ΔU, which satisfies (7).

Fig. 31(a) shows the histogram of the detection voltage variation value at the P(m, n) position, the boundary square detection voltage variation value is slightly lower than the detection voltage of the squares in the center, and the sensitivity reaches up to 20%. If the MO is located at center position P(m, n) ($m = 2, 3, 4, 5$; $n = 2, 3, 4, 5, 6, 7$), the detection sensitivity is about 19%. If the MO is located at corner position P(m, n) ($m = 1, 6$; $n = 1, 8$), the detection sensitivity is about 17.1%. To demonstrate that the magnetic induction intensity passing zero position is not a blind zone for the bipolar checkerboard MOD system, the detection voltage variation of the MO at the magnetic induction intensity passing zero position is measured. Fig. 31(b) shows the histogram of the detection voltage variation value at the P(m', n) position, which illustrates that the bipolar checkerboard MOD device can effectively eliminate the detection blind zone caused by excitation magnetic field, and the minimum sensitivity is 11%; Fig. 31(c) shows the histogram of the detection voltage variation at the P'(m', n) position, which illustrates that the bipolar checkerboard MOD device has a certain longitudinal detection capability with a voltage variation value of about 920 mV.

VI. CONCLUSION

This article analyzes the mechanism of the detection blind zone generation by the excitation magnetic field of the Tx coil. A bipolar checkerboard MOD system is proposed, which eliminates the detection blind zone from the structural design of

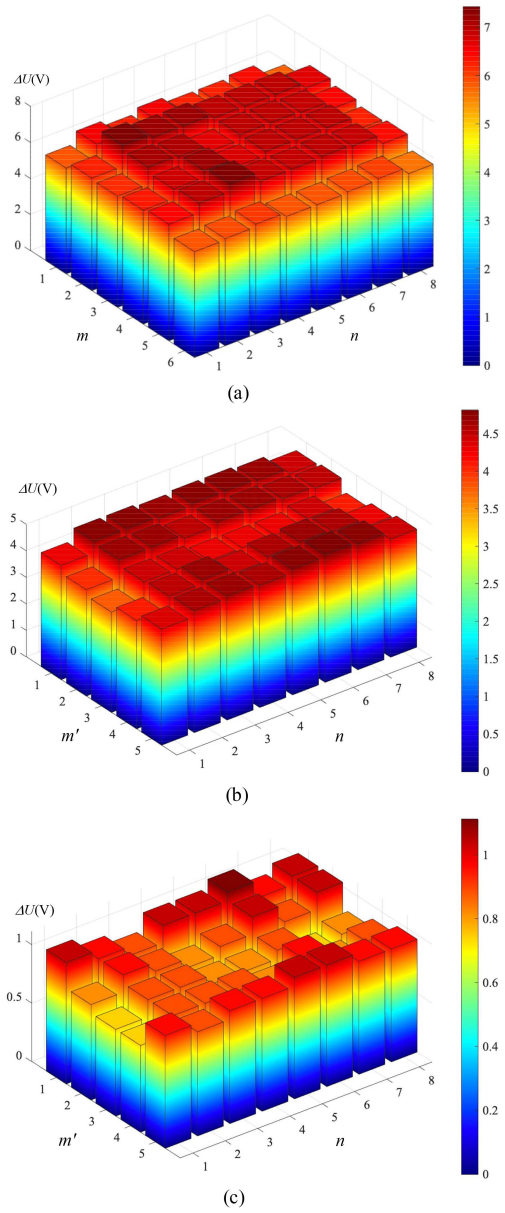

Fig. 31. Histogram of dc detection voltage variation value for MOs placed in different positions. (a) Positions of P(m, n). (b) Positions of P(m', n). (c) Positions of P'(m', n).

the MOD coil sets and realizes the independent work between the EV wireless charging system and the MOD system from the parameter design of the detection circuit. The detection of MOs can be completed before the EV wireless charging system is powered on. The MOD device is applicable to any power level of EV wireless charging device under the SAE J2954 standard, which has strong versatility, and the MOD device also has certain longitudinal MO detection capability.

REFERENCES

[1] J. Huh, S. W. Lee, W. Y. Lee, G. H. Cho, and C. T. Rim, "Narrow-width inductive power transfer system for online electrical vehicles," *IEEE Trans. Power Electron.*, vol. 26, no. 12, pp. 3666–3679, Dec. 2011.

[2] M. Sato, G. Yamamoto, D. Gunji, T. Imura, and H. Fujimoto, "Development of wireless in-wheel motor using magnetic resonance coupling," *IEEE Trans. Power Electron.*, vol. 31, no. 7, pp. 5270–5278, Jul. 2016.

[3] Z. Li, C. Zhu, J. Jiang, K. Song, and G. Wei, "A 3-kW wireless power transfer system for sightseeing car supercapacitor charge," *IEEE Trans. Power Electron.*, vol. 32, no. 5, pp. 3301–3316, May 2017.

[4] L. Zhao, D. J. Thrimawithana, U. K. Madawala, A. P. Hu, and C. C. Mi, "A misalignment-tolerant series-hybrid wireless EV charging system with integrated magnetics," *IEEE Trans. Power Electron.*, vol. 34, no. 2, pp. 1276–1285, Feb. 2019.

[5] V. Z. Barsari, D. J. Thrimawithana, and G. A. Covic, "An inductive coupler array for in-motion wireless charging of electric vehicles," *IEEE Trans. Power Electron.*, vol. 36, no. 9, pp. 9854–9863, Sep. 2021.

[6] *Electric Vehicle Wireless Power Transfer (WPT) Systems—Part 1: General Requirements*, IEC Standard 61980-1, 2020.

[7] *Wireless Power Transfer for Light-Duty Plug-In/Electric Vehicles and Alignment Methodology*, Standard SAE J2954, 2022.

[8] *Electrically Propelled Road Vehicles—Magnetic Field Wireless Power Transfer—Safety and Interoperability Requirements*, ISO Standard 19363, 2020.

[9] *Electric Vehicle Wireless Power Transfer—Part 1: General Requirements*, Standard GB/T 38775.1, 2020.

[10] S. Y. Jeong, H. G. Kwak, G. C. Jang, and C. T. Rim, "Living object detection system based on comb pattern capacitive sensor for wireless EV chargers," presented at the IEEE 2nd Annu. Southern Power Electronics Conf., Auckland, New Zealand, Dec. 5–8, 2016.

[11] T. Poguntke, P. Schumann, and K. Ochs, "Radar-based living object protection for inductive charging of electric vehicles using two-dimensional signal processing," *Wireless Power Transfer*, vol. 4, no. 2, pp. 88–97, Sep. 2018.

[12] G. C. Jang, S. Y. Jeong, H. G. Kwak, and C. T. Rim, "Metal object detection circuit with non-overlapped coils for wireless EV chargers," presented at the IEEE 2nd Annu. Southern Power Electronics Conf., Auckland, New Zealand, Dec. 5–8, 2016.

[13] X. Zhang, Y. Jin, Q. Yang, Z. Yuan, H. Meng, and Z. Wang, "Detection of metal obstacles in wireless charging system of electric vehicle," in *Proc. IEEE PELS Workshop Emerg. Technol., Wireless Power Transfer*, Chongqing, China, 2017, pp. 89–92.

[14] P. Zhang, Q. Yang, X. Zhang, Y. Li, and Y. Li, "Comparative study of metal obstacle variations in disturbing wireless power transmission system," *IEEE Trans. Magn.*, vol. 53, no. 6, Jun. 2017, Art. no. 9100304.

[15] W. Shi, J. Dong, S. Bandyopadhyay, F. Grazian, T. B. Soeiro, and P. Bauer, "Comparative study of foreign object and misalignment in inductive power transfer systems," in *Proc. 45th Annu. Conf. IEEE Ind. Electron. Soc.*, Lisbon, Portugal, 2019, pp. 2634–2639.

[16] Y. Deng, Y. Yang, Y. Luo, Z. Dai, S. Zhang, and X. Luo, "Modeling and analysis of wireless power transfer system in metal environment," in *Proc. IEEE Wireless Power Transfer Conf.*, Seoul, South Korea, 2020, pp. 252–256.

[17] X. Liu, C. Liu, W. Han, and P. W. T. Pong, "Design and implementation of a multi-purpose TMR sensor matrix for wireless electric vehicle charging," *IEEE Sensors J.*, vol. 19, no. 5, pp. 1683–1692, Mar. 2019.

[18] H. Jafari, M. Moghaddami, and A. I. Sarwat, "Foreign object detection in inductive charging systems based on primary side measurements," *IEEE Trans. Ind. Appl.*, vol. 55, no. 6, pp. 6466–6475, Nov./Dec. 2019.

[19] B. Long, Q. Zhu, S. Zang, L. Zhao, and A. P. Hu, "Metal object detection by monitoring fifth-order harmonic current of IPT system with dual frequency tuning," *IEEE Trans. Power Electron.*, vol. 37, no. 3, pp. 2513–2518, Mar. 2022.

[20] S. Y. Jeong, H. G. Kwak, G. C. Jang, S. Y. Choi, and C. T. Rim, "Dual-purpose nonoverlapping coil sets as metal object and vehicle position detections for wireless stationary EV chargers," *IEEE Trans. Power Electron.*, vol. 33, no. 9, pp. 7387–7397, Sep. 2018.

[21] L. Xiang, Z. Zhu, J. Tian, and Y. Tian, "Foreign object detection in a wireless power transfer system using symmetrical coil sets," *IEEE Access*, vol. 7, pp. 44622–44631, 2019.

[22] V. X. Thai, G. C. Jang, S. Y. Jeong, J. H. Park, Y.-S. Kim, and C. T. Rim, "Symmetric sensing coil design for the blind-zone free metal object detection of a stationary wireless electric vehicles charger," *IEEE Trans. Power Electron.*, vol. 35, no. 4, pp. 3466–3477, Apr. 2020.

[23] W. Shi, J. Dong, T. B. Soeiro, and P. Bauer, "Integrated solution for electric vehicle and foreign object detection in the application of dynamic inductive power transfer," *IEEE Trans. Veh. Technol.*, vol. 70, no. 11, pp. 11365–11377, Nov. 2021.

[24] S. Y. Chu, X. Zan, and A.-T. Avestruz, "Electromagnetic model-based foreign object detection for wireless power transfer," *IEEE Trans. Power Electron.*, vol. 37, no. 1, pp. 100–113, Jan. 2022.
[25] S. Y. Jeong, V. X. Thai, J. H. Park, and C. T. Rim, "Self-inductance-based metal object detection with mistuned resonant circuits and nullifying induced voltage for wireless EV chargers," *IEEE Trans. Power Electron.*, vol. 34, no. 1, pp. 748–758, Jan. 2019.
[26] L. Li, J. Wang, C. Cai, Z. Lin, M. Hu, and F. Zhang, "Phase-detection-based metal objects and pick-up coils detection scheme without malfunction in wireless power transfer system," *IET Elect. Power Appl.*, vol. 14, no. 11, pp. 2222–2230, Nov. 2020.
[27] T. Yong, Y. W. Lin, J. D. Tian, and L. J. Xiang, "Multi-thread sensing coil design for metal object detection of wireless power transfer systems," *Measurement*, vol. 184, Nov. 2021, Art. no. 109952.

Shuze Zhao received the B.S. degree in electrical engineering in 2018 from China University of Mining and Technology, Xuzhou, China, where he is currently working toward the Ph.D. degree in electrical engineering with the School of Electrical Engineering.

His current research focuses on wireless power transfer.

Chenyang Xia (Member, IEEE) was born in Jiangsu Province, China, in 1982. He received the B.S., M.S., and Ph.D. degrees in control theory and control engineering from Chongqing University, Chongqing, China, in 2006, 2008, and 2010, respectively.

From 2018 to 2019, he was an Academic Visitor with the University of Auckland, Auckland, New Zealand. He is currently a Professor with the School of Electrical Engineering, China University of Mining and Technology, Xuzhou, China. His research interests include wireless power transfer and intelligent control.

Ziyue Yang received the B.S. degree in electrical engineering in 2020 from China University of Mining and Technology, Xuzhou, China, where he is currently working toward the Ph.D. degree in electrical engineering with the School of Electrical Engineering.

His current research focuses on wireless power transfer.

Hao Lu received the B.S. degree in electrical engineering from Soochow University, Suzhou, China, in 2020. He is currently working toward the M.S. degree in electrical engineering with the School of Electrical Engineering, China University of Mining and Technology, Xuzhou, China.

His current research focuses on wireless power transfer.

Hongtai Zhang received the B.S. degree in electrical engineering in 2020 from China University of Mining and Technology, Xuzhou, China, where he is currently working toward the M.S. degree in electrical engineering with the School of Electrical and Power Engineering.

His current research focuses on wireless power transfer.

Chenhao Lu received the B.S. degree in electrical engineering in 2022 from China University of Mining and Technology, Xuzhou, China, where he is currently working toward the M.S. degree in electrical engineering with the School of Electrical Engineering.

His current research focuses on wireless power transfer.